Time-lapse imaging of saline-tracer transport in fractured rock using difference-attenuation radar tomography

Frederick D. Day-Lewis,[1,2] John W. Lane, Jr.,[3] Jerry M. Harris,[4] and Steven M. Gorelick[5]

Received 17 September 2002; revised 20 May 2003; accepted 28 July 2003; published 18 October 2003.

[1] Accurate characterization of fractured-rock aquifer heterogeneity remains one of the most challenging and important problems in groundwater hydrology. We demonstrate a promising strategy to identify preferential flow paths in fractured rock using a combination of geophysical monitoring and conventional hydrogeologic tests. Cross-well difference-attenuation ground-penetrating radar was used to monitor saline-tracer migration in an experiment at the U.S. Geological Survey Fractured Rock Hydrology Research Site in Grafton County, New Hampshire. Radar data sets were collected every 10 min in three adjoining planes for 5 hours during each of 12 tracer tests. An innovative inversion method accounts for data acquisition times and temporal changes in attenuation during data collection. The inverse algorithm minimizes a combination of two functions. The first is the sum of weighted squared data residuals. Second is a measure of solution complexity based on an a priori space-time covariance function, subject to constraints that limit radar-attenuation changes to regions of the tomograms traversed by high difference-attenuation ray paths. The time series of tomograms indicate relative tracer concentrations and tracer arrival times in the image planes; from these we infer the presence and location of a preferential flow path within a previously identified zone of transmissive fractures. These results provide new insights into solute channeling and the nature of aquifer heterogeneity at the site. *INDEX TERMS:* 0910 Exploration Geophysics: Data processing; 0915 Exploration Geophysics: Downhole methods; 1829 Hydrology: Groundwater hydrology; 1832 Hydrology: Groundwater transport; 1894 Hydrology: Instruments and techniques; *KEYWORDS:* radar tomography, fractured rock, ground-penetrating radar, geophysics, hydrogeophysics

Citation: Day-Lewis, F. D., J. W. Lane, Jr., J. M. Harris, and S. M. Gorelick, Time-lapse imaging of saline-tracer transport in fractured rock using difference-attenuation radar tomography, *Water Resour. Res.*, *39*(10), 1290, doi:10.1029/2002WR001722, 2003.

1. Introduction

[2] Recent advances in geophysical exploration technology and interpretation methods have enabled high-resolution monitoring of natural hydrologic processes, hydraulic tests, and tracer experiments. The combination of time-lapse tomographic imaging and conventional hydrogeologic measurements reduces the ambiguity involved in relating geophysical data to the aquifer properties of interest. Difference tomography, in which tomograms show changes from some background image or data set, directly reveals changes in such quantities as water content and salinity. Use of this information as calibration data for numerical flow and transport models is a promising strategy for improving the reliability of model predictions. Additional calibration data are especially needed in fractured-rock settings, where aquifer heterogeneity and preferential flow paths are exceedingly difficult to identify based on traditional hydrogeologic methods [*National Research Council*, 1996]. For this purpose, cross-borehole ground-penetrating radar (GPR) has proven particularly useful.

[3] Examples of environmental and engineering applications of time-lapse geophysical monitoring are increasingly prominent in the literature. We limit our summary to a few pertinent studies. Electrical methods have been used to monitor tracer migration [*Singha et al.*, 2003; *Slater et al.*, 2000, 1997; *White*, 1988; *Osiensky and Donaldson*, 1995], contaminant leaks [*Binley et al.*, 1997; *Ramirez et al.*, 1996], steam injection [*Ramirez et al.*, 1993], and tide-driven salinity changes [*Slater and Sandberg*, 2000]. Time-lapse seismic methods have been used to monitor primary petroleum production [*Burkhart et al.*, 2000], tidal fluctuation [*Bachrach and Nur*, 1998], and enhanced oil recovery [*Harris et al.*, 1996a, 1996b]. *Brewster and Annan* [1994] and *Brewster et al.* [1995] used GPR to monitor the release of a dense nonaqueous phase liquid. Cross-well radar has been used to monitor changes in soil moisture [e.g., *Eppstein and Dougherty*, 1998a; *Binley et al.*, 2001], injections of vegetable oil emulsion for biostimulation [*Lane et al.*, 2003], and tracer tests in sedimentary aquifers [*Hubbard et al.*, 2001]. Electromagnetic tomography also has been used to study oil-shale retorts [*Daily*, 1984] and changes in moisture in fractured rock [*Daily and Ramirez*, 1989]. Difference-attenuation radar tomography has been

[1]Department of Geology, Bucknell University, Lewisburg, Pennsylvania, USA.
[2]On leave at the Office of Ground Water, Branch of Geophysics, U.S. Geological Survey, Storrs, Connecticut, USA.
[3]Office of Ground Water, Branch of Geophysics, U.S. Geological Survey, Storrs, Connecticut, USA.
[4]Department of Geophysics, Stanford University, Stanford, California, USA.
[5]Department of Geological and Environmental Sciences, Braun Geology Corner, Stanford University, Stanford, California, USA.

0043-1397/03/2002WR001722

used to monitor injections of electrically conductive tracers at a number of fractured-rock research sites [*Olsson et al.*, 1992, 1991; *Niva et al.*, 1988; *Ramirez and Lytle*, 1986].

[4] Traditionally, difference-tomography studies have used a single time set of difference data to invert each difference tomogram. In the case of multiple snapshots, each tomogram was inverted independently [e.g., *Hubbard et al.*, 2001; *Lane et al.*, 2000; *Olsson et al.*, 1991]. These analyses rely on the assumption that changes in the imaged property are negligible during the time interval of data collection. In the case of long-duration tracer tests [e.g., *Olsson et al.*, 1991], this is a safe assumption. However, for short-duration tracer tests where solute concentrations change quickly relative to tomographic data collection [e.g., *Lane et al.*, 2000], this assumption may introduce significant error [*Day-Lewis et al.*, 2002]. In addition, regularization methods for single-snapshot inversion do not take advantage of the four-dimensional (4-D) nature of the data set and target anomaly.

[5] To the best of our knowledge, no previous field-scale study has fully combined difference radar tomography and controlled tracer tests to infer tracer arrival time in multiple image planes. Traditionally in time-lapse tomography, there has been an unfortunate trade-off between two conflicting objectives: (1) acquisition of adequate ray path coverage in each time-lapse data set, and (2) minimizing the time over which each data set is collected, so that changes in concentration are negligible during acquisition. Inversion may result in poor-quality tomograms either if the ray path coverage is poor or if data are inconsistent due to temporal changes. Consequently, previous applications of time-lapse imaging to tracer test monitoring were limited to the production of a few time-lapse images during long-duration tracer tests.

[6] The goals of this paper are (1) to demonstrate innovative experimental and inversion approaches for difference-attenuation radar monitoring of time-varying phenomena, (2) to obtain high spatial and temporal resolution images of field-scale tracer migration, and (3) to gain new basic and site-specific insights into field-scale solute transport in fractured media. Toward these ends, we employ an experimental procedure involving sequential injection and incremental scanning [*Lane et al.*, 1998, 2000] and apply an innovative inversion method for time-varying phenomena [*Day-Lewis et al.*, 2002]. The inversion accounts for precise measurement times, uses multiple time sets of data to invert each tomogram, and capitalizes on temporal correlation to regularize the inversion. Furthermore, the method allows for ray-based constraints to restrict difference-attenuation anomalies to regions of the tomogram traversed by ray paths along which large increases in attenuation occur. For under-determined problems, such additional constraints can enhance model resolution. *Day-Lewis et al.* [2002] demonstrated this methodology using a synthetic example based loosely on data presented here and showed that it produced superior results compared with independent inversion of snapshot tomograms. We apply the method to new experimental data from the U.S. Geological Survey Fractured Rock Hydrology Research Site, near Mirror Lake in Grafton County, New Hampshire. Radar data were collected in three image planes during a series of tracer tests. We invert the data on a sequence of time-lapse 3-D nodal meshes to generate a time series of difference-attenuation tomograms.

[7] The results of our time-lapse inversion provide new insight into aquifer heterogeneity and solute transport at the Mirror Lake Site. In previous analyses of hydraulic data from the Mirror Lake Site, numerical flow models were successfully calibrated assuming that fracture zones were internally homogeneous [*Day-Lewis et al.*, 2000; *Hsieh et al.*, 1999]. Recent interpretation of tracer test data from the site suggests the role of permeability heterogeneity in tailing behavior [*Becker and Shapiro*, 2003, 2000]; however, the permeability structure between wells is difficult or impossible to identify based only on hydrologic data. Our geophysical results provide high-resolution information about solute channeling and heterogeneity within a fracture zone. Time-lapse tomograms indicate relative tracer concentrations and tracer arrival times in the three image planes. Inference of field-scale channelized transport would not be possible without the aid of time-lapse geophysical imaging.

2. Background

2.1. Site Description

[8] We conducted a series of experiments in the Forest Service East (FSE) well field at the U.S. Geological Survey (USGS) Fractured Rock Hydrology Research Site located near Mirror Lake in Grafton County, New Hampshire (Figure 1). The results of this experiment have not been fully presented previously. The FSE well field is a 120-m $\times$ 80-m area consisting of 14 boreholes. The bedrock underlying the area is schist intruded by granite, pegmatite and lamprophyre, and is overlain by approximately 20 m of glacial deposits. *Hsieh and Shapiro* [1996] identified four highly transmissive fracture zones that dominate the hydraulic behavior of the site. During pumping tests, wells connected by a fracture zone exhibit similar drawdown responses, whereas wells not connected by a fracture zone show different responses. Each zone connects four or more wells. On the basis of hydraulic data and calibration of groundwater flow models, the zones are tabular, subhorizontal features that extend several tens of meters and have permeability about 4 orders of magnitude higher than that of the surrounding bedrock [*Day-Lewis et al.*, 2000; *Hsieh et al.*, 1999].

2.2. Radar Tomography

[9] In cross-well radar or seismic tomography [*Dines and Lytle*, 1979; *Nolet*, 1987], waves are transmitted from sources in one borehole to receivers in one or more boreholes. Waveform data are recorded and processed to yield quantities such as travel time, energy, or amplitude for each waveform trace. Tomographic inversion of the processed data generates images of slowness, attenuation, or other quantities in the interwell region. In the case where wave propagation dominates over conduction, radar velocity is approximated by equation (1) and radar attenuation by equation (2) [e.g., *Stratton*, 1941, pp. 275–277; *Davis and Annan*, 1989]:

$$v \approx \frac{c}{\sqrt{\varepsilon_r}} \tag{1}$$

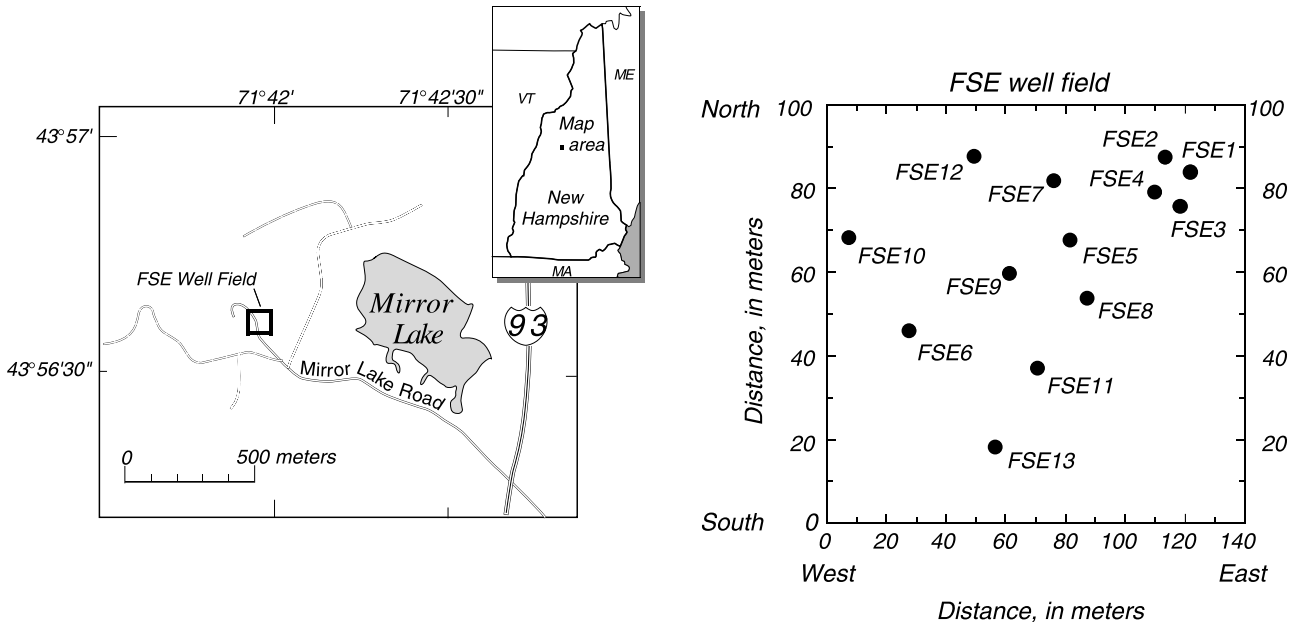

Figure 1. Map of the U.S. Geological Survey Fractured Rock Hydrology Research Site near Mirror Lake, in Grafton County, New Hampshire.

where v is radar velocity [m/s], c is the velocity of electromagnetic waves in a vacuum [m/s], and ε_r is the dielectric permittivity of the medium, relative to a vacuum;

$$\alpha \approx 0.163\sigma/\sqrt{\varepsilon_r} \tag{2}$$

where α is the attenuation [dB/m] and σ is electrical conductivity [μS/cm]. According to equation (2), radar attenuation is directly proportional to electrical conductivity, which increases with pore-fluid salinity [*Archie*, 1942]; thus saline tracer tests can illuminate preferential pathways and permeable fractures for radar imaging.

[10] For most problems in seismic tomography, velocity contrasts are significant, ray bending according to Snell's law cannot be neglected, and tomographic inversion is necessarily nonlinear; however, in radar tomography, velocity contrasts are typically small, and the straight-ray assumption is often justified. *Olsson et al.* [1992] suggest that ray bending can be neglected for contrasts less than 10–15%. We estimate velocity contrasts for our data set to be of the order of 5% and estimate changes during the test to be much less. Changes in ray paths due to saline tracer migration are usually ignored [*Olsson et al.*, 1991], as radar velocity is not strongly affected by salinity.

[11] Geotomographic inverse problems require solution of large, under-determined, or mixed-determined systems of equations. Additional information is typically necessary to regularize the inverse problem. Prior information typically consists of ad hoc damping, flatness, or smoothness criteria [*Menke*, 1989]. In severely under-determined problems, poor model resolution may result in blurring or streaking artifacts. Strategies to assess or minimize inversion artifacts and model ambiguity include (1) approaches to constrain anomalies to a small number of homogenous zones [*Hyndman and Harris*, 1996; *Hyndman et al.*, 1994; *Eppstein and Dougherty*, 1998b]; (2) parsimonious parameterization based on sta and adapted grids [*Vesnaver and Böhm*, 1999, 2000], natural pixels [*Michelena and Harris*, 1991], or a geometric description of the expected target anomaly [*Lane et al.*, 2003]; (3) stochastic regularization [*Maurer and Holliger*, 1998]; and (4) use of additional ray-based constraints to restrict the extent of anomalies [*Singh and Singh*, 1991; *Day-Lewis et al.*, 2002]. In this paper we adapt the time-lapse inversion approach of *Day-Lewis et al.* [2002] for application to field data collected in multiple adjoining planes. In contrast to other approaches, this method accounts for temporal variations of the target anomaly and the timing of measurements, which are critical for problems where solute concentrations change quickly relative to data acquisition.

3. Field Experiment

3.1. Setup

[12] Cross-well radar tomography was used to monitor tracer experiments in a zone of transmissive fractures in the FSE1-FSE4 well cluster (Figure 1), in the northeast corner of the FSE well field. On the basis of hydraulic tests, *Hsieh and Shapiro* [1996] determined that fractures intersect and hydraulically connect the four boreholes at about 45-m depth, about 25 m below the overburden-bedrock interface. We conducted a series of weak-doublet tracer tests, in which fluid was pumped continuously at 3.8 L/min from FSE4 and injected continuously at 1.9 L/min in FSE1. The 2:1 ratio of pumping-to-injection was chosen to prevent migration of the saline tracer off-site. After achieving steady state flow, the injection fluid was switched for 10 min from freshwater to a sodium-chloride (NaCl) tracer with a concentration of 50 g/L NaCl, or 30 g/L Cl. Although the tracer fluid is denser than the native groundwater, we expect density effects on flow to be minor given the large permeability contrasts at the site and the relatively high pumping rate. Injection of freshwater was resumed after the 10-min period. The specific conductance of the freshwater averaged about

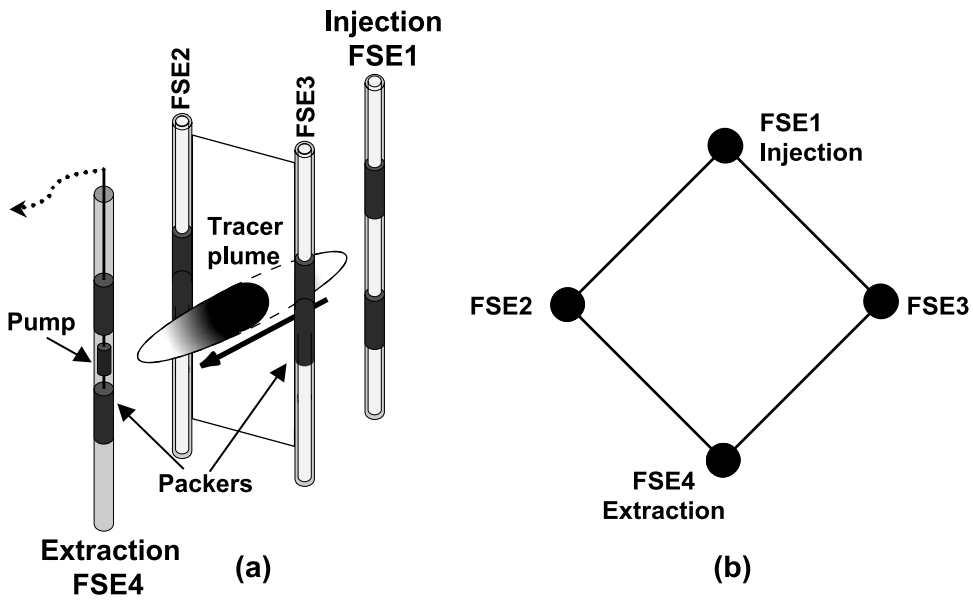

Figure 2. (a) Cross section and (b) plan view of the experimental setup for the cross-hole radar and tracer experiments. Tracer injection was in FSE1, extraction was from FSE4, and tomographic imaging was in the FSE1-FSE2, FSE2-FSE3, and FSE3-FSE1 planes. The distance between injection and extraction wells is about 13 m. Not to scale.

400 μS/cm, which approximated the specific conductance of ground water. The specific conductance of the tracer could not be measured with our field probe, but is estimated to be 67,580 μS/cm based on regression of tabulated data from *Dakhnov* [1962].

[13] Hydraulic packers were used to isolate the fracture zone, prevent vertical flow in boreholes, and preclude saline water from entering FSE2 and FSE3 (Figure 2). Special log-through PVC packers and core pipe were used in FSE1, FSE2, and FSE3 to permit cross-hole imaging in the FSE1-FSE2, FSE2-FSE3, and FSE3-FSE1 planes. The use of conventional packers was required in FSE4 due to the presence of the pump, which precluded placement of radar antennas in FSE4. The discharge water at FSE4 was sampled at 10-min intervals for the first 4 hours of each tracer test, and at 30-min intervals thereafter. The chloride concentration history at FSE4 for one tracer test is shown in Figure 3. The concentration history shows two peaks; the first is sharper and larger in magnitude than the second peak. The maximum chloride concentration observed at the outlet, 1 g/L, is about 1/30th of the injection concentration, presumably due to dispersion and dilution.

3.2. Radar-Data Acquisition

[14] Most commercially available borehole-radar systems are single-channel, which severely constrains the rate of data acquisition. In order to collect sufficient radar data to provide good ray path coverage between wells, we employed the sequential injection and incremental scanning (SIIS) procedure developed by *Lane et al.* [1998]. For each of the three image planes, this entailed conducting four tracer tests and collecting radar data for a different transmitter-receiver geometry at 10-min intervals during each test; thus a different portion of the interwell region was scanned during each of 12 tracer tests. Figure 4 illustrates the data acquisition proc for the FSE1-FSE2 plane, which occurred over four consecutive days. For this plane, each of the four transmitter-receiver geometries (Figures 4a, 4b, 4c, 4d) comprised three common-transmitter or common-receiver gathers. The data from the four geometries are combined (Figure 4e) to produce a complete time-lapse data set for the FSE1-FSE2 plane. Although data collection for each geometry was begun at 10-min intervals, the actual time required varied from about 4 to 8 min, depending on the particular common-antenna gathers collected. After 5 hours of data collection, the antenna batteries were recharged for 3 hours and another data set was collected. Thus data were collected to produce 31 time-lapse tomograms.

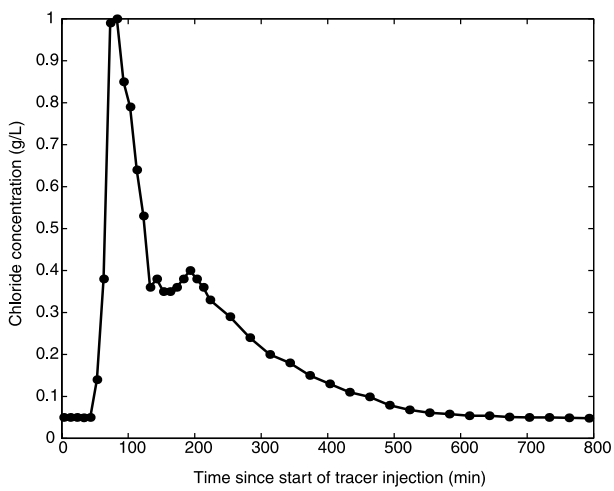

Figure 3. Tracer concentration measurements in discharge water at FSE4.

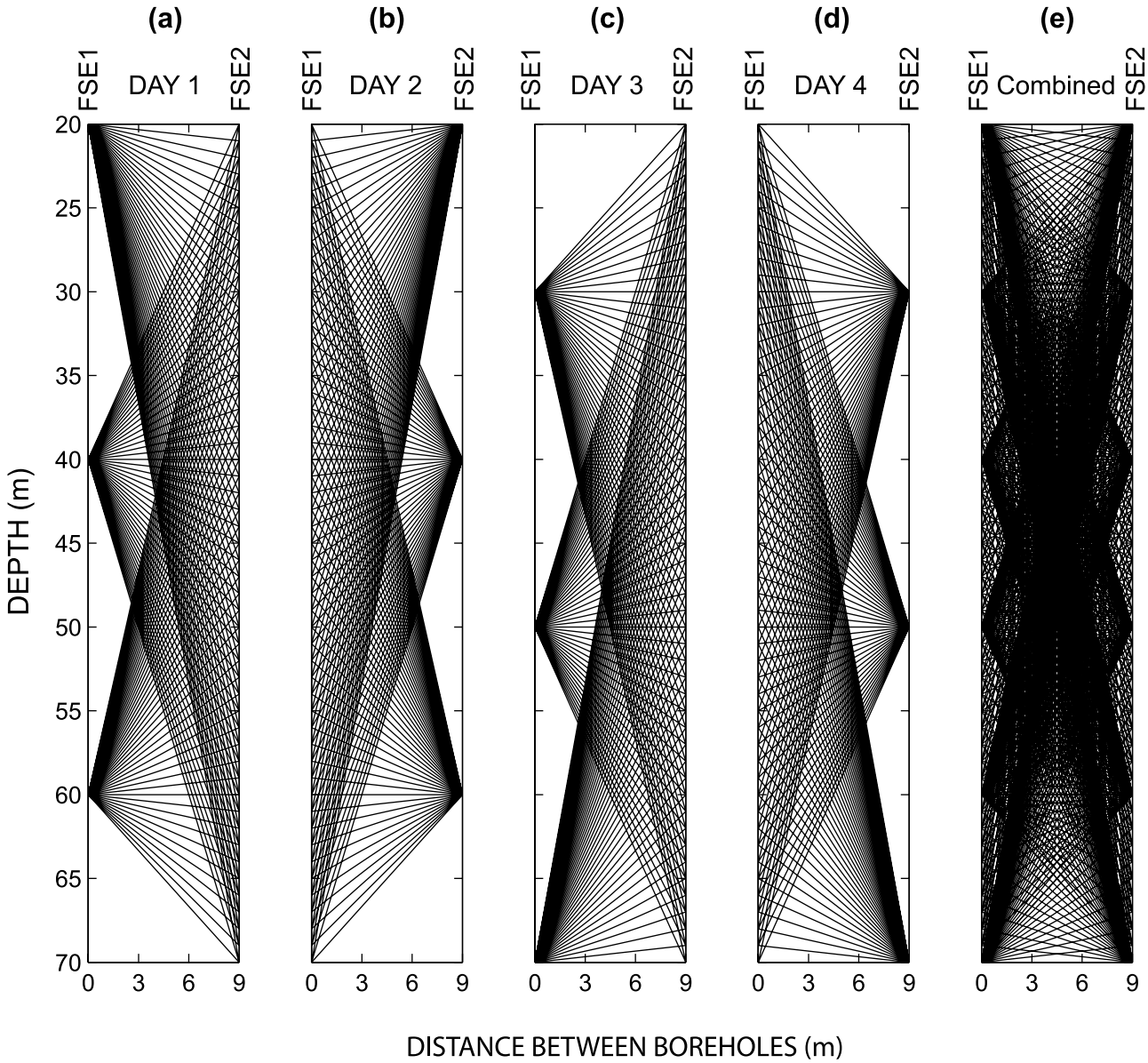

Figure 4. (a–d) Transmitter-receiver patterns for radar scanning in the FSE1-FSE2 plane during four tracer tests, and (e) the combined ray path coverage. Every fourth ray path is plotted for purpose of clarity.

[15] Before the start of each tracer test, a complete data set including all geometries was collected. These data sets provide the ''background'' data for differencing. By differencing each time-lapse data set against its respective background set, the effects of any changes in background salinity are minimized. Comparison of specific conductance histories for various tests indicates similar concentration histories.

[16] Cross-well data were collected using a MALÅ GeoScience RAMAC radar system with 100 MHz electric dipole antennas. (The use of trade, brand, or firm names in this paper is for identification purposes only and does not constitute an endorsement by the U.S. Geological Survey.) Using a sampling frequency of 1937 MHz, 1024 samples were collected for each trace. For each sample, 16 measurements were stacked (averaged). Data for the FSE2-FSE3 plane were acquired i ber of 1997, and data for the FSE1-FSE2 and FSE3-FSE1 planes were collected in October of 1998. Antennas were positioned in all wells between depths of 20 and 70 m from the top of the respective well casings. In the FSE2-FSE3 plane, a vertical increment of 0.5 m between antenna positions was used. Improvements in data acquisition procedures in October of 1998 permitted use of a finer, 0.25-m vertical increment in the FSE1-FSE2 and FSE3-FSE1 planes.

[17] On the basis of an average velocity of 130 m/μs and dominant frequency of 100 MHz, we estimate the wavelength to be about 1.3 m. Given the separation distance and vertical extent of the boreholes bounding a tomogram, the theoretical limits of vertical and horizontal resolution for transmission tomography can be estimated according to the formulae of *Schuster* [1996]. In the FSE2-FSE3 planes, the horizontal resolution is estimated to be 1.3 m and the vertical resolution to be 2.9 m. It should be noted that other

factors including measurement error, regularization, and finite ray coverage could degrade the resolution. Other discussions of tomographic resolution include those of *Rector and Washbourne* [1994], *Williamson and Worthington* [1993], and *Bregman et al.* [1989a, 1989b].

3.3. Previous Results

[18] Initial tomographic inversions were performed by *Lane et al.* [1998] using a ray-projection technique algorithm [*Singh and Singh*, 1991] for the FSE2-FSE3 plane and by *Lane et al.* [1998] using weighted-damped least squares for the FSE1-FSE2 and FSE3-FSE1 planes. Tomograms indicated the presence of a preferential flow path from FSE1 to the vicinity of FSE2. These initial results provided preliminary insights into the control of heterogeneity on solute transport at the FSE well field; however, tomographic results were difficult to interpret in two respects. First, tomograms contained streak artifacts owing to poor model resolution arising from the trade-off between spatial and temporal sampling [*Lane et al.*, 2000]. Such artifacts could easily be misinterpreted as fractures transporting tracer. Second, the plots of pixel difference-attenuation versus time were noisy because changes during the 10-min data acquisition interval were neglected and no temporal regularization was applied in the inversion. Thus estimation of tracer peak arrival time was problematic.

[19] In this paper we employ several strategies to address these problems. We combine data from multiple planes and time steps and apply ray-based constraints in a more rigorous manner to improve model resolution and reduce artifacts. To further suppress artifacts and impose smoothness in time, we use space-time regularization [*Day-Lewis et al.*, 2002]. Finally, we account for concentration changes during data collection to reduce errors arising from the static-image assumption.

4. Mathematical Methods

4.1. Data Processing

[20] Raw waveform data are processed ray by ray to calculate difference data sets that are inverted to generate images of difference attenuation. Analysis of difference data is preferred to differencing inverted images of absolute attenuation for three reasons. First, the analysis of difference data does not require knowledge of the transmitter and receiver radiation patterns. Second, it allows us to account for data acquisition times as discussed in the following sections. Third, examination of difference data provides insights into establishing constraints on anomaly location and extent. The difference attenuation d_i^k, measured for ray path i in time-lapse data set k, is calculated in decibels (dB) as

$$d_i^k = 10 \times \log_{10}\left[\frac{\sum_{j=1}^{n\text{samples}} \left(A_{ij}^0\right)^2}{\sum_{j=1}^{n\text{samples}} \left(A_{ij}^k\right)^2}\right] \quad (3)$$

where A_{ij}^0 is the amplitude of sample j for trace i in the background data set; A_{ij}^k is the amplitude of sample j for trace i in the current time k data set; and $n$samples is the number of samples for the trace. Whereas the attenuation of the medium, α, has units of dB/m, the difference-attenuation data are integrated measurements of α along the ray path and thus have units of decibels.

[21] To collect a common-transmitter or common-receiver gather, one antenna was held at a constant depth, while the other was either lowered or raised between 70- and 20-m depth. Although the starting location of the moving antenna was accurately set for each gather, the ending location was typically several centimeters from the desired final depth. These centimeter-scale errors in antenna locations were apparent in plots of trace energy data (e.g., Figure 5a), where the time-lapse and background amplitude curves showed apparent offsets in depth, but were otherwise similar, suggesting antenna location error. Differencing two offset data sets would produce spurious attenuation differences and could result in large errors in tomograms. To overcome antenna location error we use a search algorithm to relocate the final antenna locations for each time-lapse data set. The processed, corrected data are then reviewed to ensure that important information about attenuation changes is not eliminated by the relocation procedure.

[22] The objective of the search algorithm is to find the set of antenna locations (assuming a constant depth increment between locations) that minimizes the differences between the time-lapse data and the background, reference data. The search algorithm adjusts the final location of the moving antenna in small increments within a reasonable tolerance. For each candidate final location, the actual depth interval between antenna locations is calculated, and data are interpolated at the desired locations (i.e., from 20- to 70-m depth in 0.25-m increments) for comparison with the background data set. The optimal solution identifies the final antenna location that minimizes the sum of squared amplitude differences between the interpolated time-lapse data and the background data set. For this problem, we tested final antenna locations in increments of 6.25 cm within a 1-m window centered on the expected location. For example, in the FSE1-FSE2 plane, data were collected from 20-m depth to 70-m depth at 0.25-m intervals. Our search algorithm tested final antenna locations from 69.5 to 71.5 m in 6.25-cm increments. For each possible location, processed ray data are interpolated to the desired locations (i.e., 20- to 70-m depth in 0.25-m increments). The final location that yields the best match to the background data set is taken as the true ending location.

[23] Exploratory analysis of difference-attenuation data can provide valuable insights into tracer transport before rigorous tomographic inversion. Trace-energy and difference-attenuation data are plotted for 100 traces from the FSE1-FSE2 data set in Figures 5a and 5b. The effect of the tracer is evident in a small subset of the data. The experimental data clearly indicate temporal changes in the magnitude of tracer concentration along certain ray paths; the presence of the saline tracer reduces trace energy by more than 10 dB for some ray paths, whereas other ray paths are unaffected. Comparison of data collected at different times indicates the tracer concentration in the FSE1-FSE2 plane peaks at about 20 min after the start of tracer injection (10 min after cessation) and drops quickly thereafter.

[24] To visualize the spatial distribution of tracer at different times, plots of high and low difference-attenuation

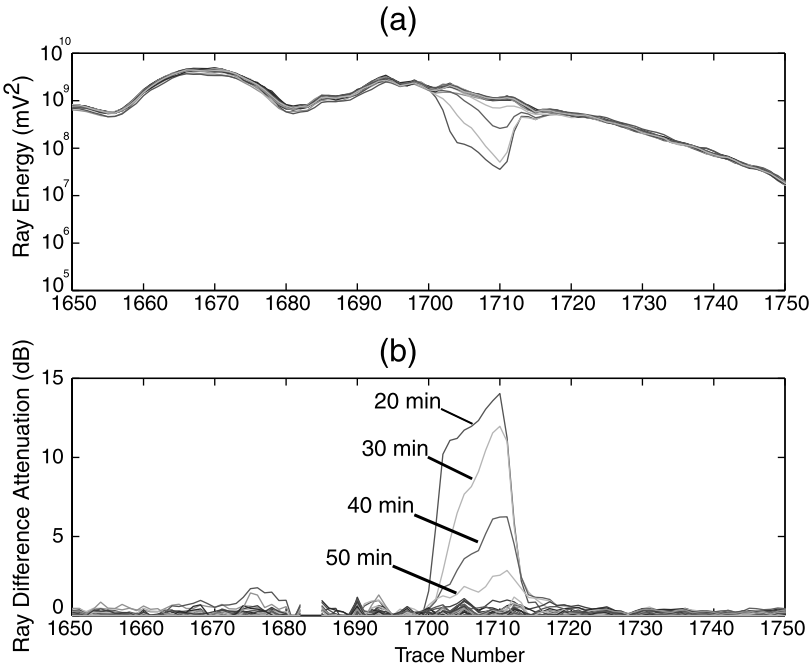

Figure 5. Processed data for 100 ray paths in the FSE1-FSE3 plane, with the antenna in FSE3 held at 200.57 m and the antenna in FSE1 moving from 209.01 m to 184.02 m. (a) Ray energy, calculated as the sum of amplitude squared over each trace, and (b) ray difference-attenuation data.

ray paths are useful. Figure 6a shows the ray paths in the FSE2-FSE3 plane for difference-attenuation data values in excess of the 95th percentile for the 70-min data set. Figure 6b shows the ray paths for difference-attenuation data with values less than the mean for the same data set. Ray paths in Figure 6a are strongly affected by the tracer, whereas the ray paths in Figure 6b are largely unaffected. Comparison of these two figures indicates that tracer migration is confined to a small region of the FSE2-FSE3 cross section, in the vicinity of FSE2. Such insights can be utilized to develop ray-based constraints for under-determined inverse problems [*Day-Lewis et al.*, 2002].

[25] A third exploratory analysis of the data entails examination of plots of difference-attenuation versus time for different ray paths. Difference-attenuation histories for several high and low difference-attenuation ray paths are shown in Figure 7. As expected, the largest changes in difference attenuation are seen in rays that cross the injection zone in the FSE1-FSE2 and FSE3-FSE1 planes. Again, the target anomaly reaches a maximum attenuation in these planes at about 20 min after the start of tracer injection. The difference attenuation in the FSE2-FSE3 plane exhibits a lower, broader peak at a later time, as expected based on the configuration of wells and nature of the doublet tracer test, in which fluid is continuously injected and extracted. The tracer plume is more disperse by the time it reaches the FSE2-FSE3 cross section. The attenuation change in the FSE3-FSE1 plane drops off quickly, whereas the anomaly in the FSE1-FSE2 plane persists because the tracer passes through the FSE2-FSE3 plane near FSE2.

4.2. Parameterization

[26] We apply the approach of *Day-Lewis et al.* [2002] for space-time parameterization in time-lapse tomography to field data for the first t d adapt the method for use with data from multiple planes between deviated wells. The model parameters to be estimated are difference-attenuation values at nodes in a 4-D mesh. A nodal mesh is better suited to accounting for 3-D well deviation and 4-D interpolation than is the more commonly applied pixelated grid. In pixelated grids, parameter values are assumed constant within a pixel. In the nodal mesh, values are interpolated in between nodes for ray tracing and display, allowing for smooth variation in time. With a nodal mesh, it is possible to confine estimated parameters to deviated image planes, resulting in fewer parameters to estimate and a more uniform ray density.

[27] The 4-D mesh consists of a time series of identical 3-D spatial meshes. For a synthetic two-dimensional (2-D) time-lapse problem, *Day-Lewis et al.* [2002] used bilinear interpolation to find difference attenuation between nodes in order to construct a forward model. In the case of multiple wells with vertical deviations, this method is cumbersome and requires construction of a 3-D spatial mesh such that the mesh would contain all ray paths in the image planes. In this study, the 3-D spatial mesh is constructed by connecting three deviated 2-D meshes, with one 2-D mesh for each image plane (Figure 8a). We use a constant vertical spacing between layers of nodes, with a set number of nodes in each image plane. The distances between wells, which are slightly deviated, determines the horizontal spacing between nodes. Ray paths are not confined to best fit vertical planes between wells; rather, difference-attenuation values at points along ray paths are interpolated from values as nearby nodes. Because the magnitude and location of anomalies varies greatly between planes, we estimate difference attenuation at a point using only nodes in the corresponding deviated image plane containing the point.

[28] The difference attenuation of the medium (current minus background attenuation), $\Delta\alpha(\mathbf{x}, t)$, at a given point in

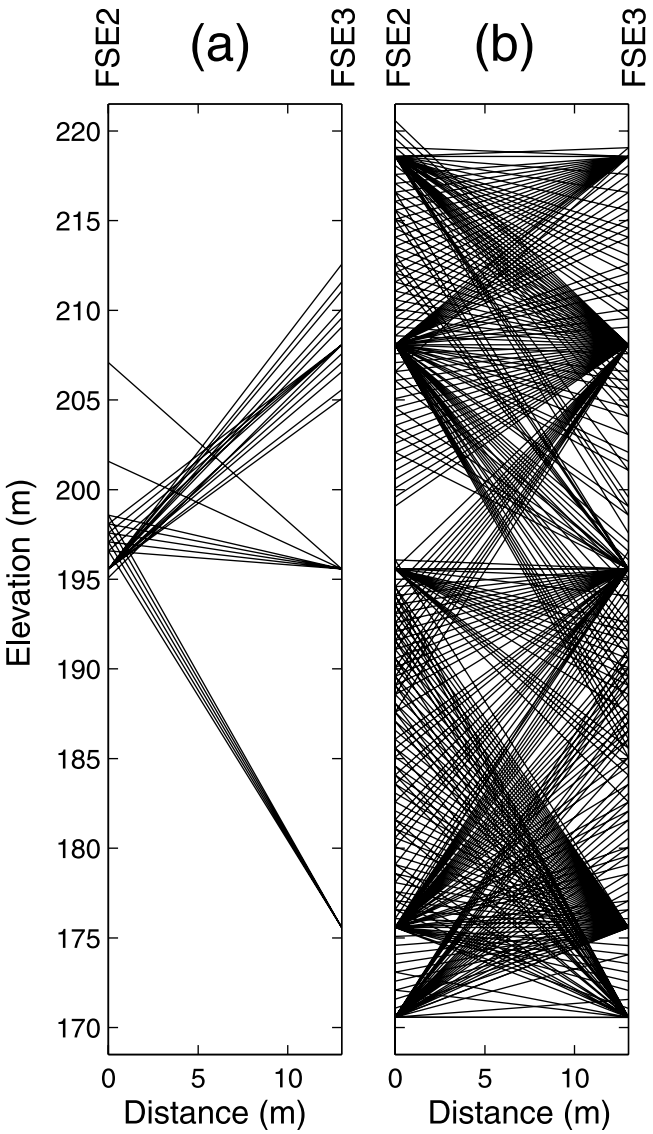

Figure 6. Plots of (a) high and (b) low difference-attenuation rays in the FSE2-FSE3 plane.

space and time is modeled as a weighted average of difference-attenuation values at nodes within a space-time neighborhood containing the point:

$$\Delta\alpha(\mathbf{x},t)=\sum_{k=k1}^{k2}\sum_{j=1}^{mnodes} w_j^k(\mathbf{x},t)\Delta\alpha_j^k \tag{4}$$

where $w_j^k(\mathbf{x}, t)$ is the weight at location $(\mathbf{x}, t)$ of node j at mesh time T^k; $\Delta\alpha_j^k$ is the difference attenuation of node j at mesh time T^k, in dB/m; and $k1$, $k2$ are mesh-time indices such that $T^{k1} < t < T^{k2}$.

[29] Interpolation is performed locally, within mesh layers, for each cross-sectional plane, so that simulated data for ray paths in one plane are not functions of nodes in another plane. Interpolation at a point, $(\mathbf{x}, t)$, involves four nodes in the mesh for time T^k and four in the mesh for time T^{k+1}, such that $T^k < t < T^{k+1}$. The four nodes in each time mesh include the two closest nodes in the z-layer directly below and above $\mathbf{x}$ in the appropriate image plane. Thus interpolation along a give path only utilizes nodes in the plane in which the measurement was collected. We use inverse-squared-distance interpolation in both space and time [e.g., *Isaaks and Srivastava*, 1989]:

$$w_j^k(\mathbf{x},t)=\frac{\left(t-T^k\right)^{-2}}{\sum_{\substack{l\in \text{closest}\\ \text{two mesh}\\ \text{times}}}\left(t-T^l\right)^{-2}}\cdot\frac{\|\,\mathbf{x}-\mathbf{x}_j\,\|^{-2}}{\sum_{\substack{n\in \text{closest}\\ \text{four nodes}\\ \text{in space}}}\|\,\mathbf{x}-\mathbf{x}_n\,\|^{-2}} \tag{5}$$

where $w_j^k(\mathbf{x}, t)$ is the weight of node j in the k-time mesh at space-time location $(\mathbf{x}, t)$. Inverse-distance weights are easily calculated for irregular meshes. Discontinuities are possible at cell boundaries using this method, but for test cases, this did not greatly impact inverse solutions compared with solutions using bilinear interpolation. For local interpolation on a sufficiently fine mesh, similar results are expected regardless of the interpolation scheme.

4.3. Forward Model

[30] On the basis of our space-time parameterization, each measurement is a function of the difference attenuation at nodes in two time meshes. The measured difference attenuation (in dB) is modeled as the line integral of difference attenuation of the medium (in dB/m) along the ray path (in m) [*Day-Lewis et al.*, 2002]:

$$\hat{d}_i^k=\int_{R_i}\Delta\alpha\left(\mathbf{r},t_i^k\right)dr\approx\sum_{j=1}^{nnodes}G_{ij}^{k,k}\Delta\alpha_j^k+\sum_{j=1}^{mnodes}G_{ij}^{k,k+1}\mathrm{a}_j^{k+1} \tag{6}$$

where

$\hat{d}_i^k$ simulated difference energy for ray i in the k-time data set (dB);
$\mathbf{r}$ point in space along the ray path R_i;
t_i^k collection time for ray path i in the k-time data set;
$G_{ij}^{k,l}$ influence of node j in the T^l-time mesh on ray i in the k-time data set.

The elements of the ray path matrices, $\mathbf{G}^{k,k}$ and $\mathbf{G}^{k,l}$, describe the linear sensitivities of simulated difference-attenuation measurements in data set k to nodal difference-attenuation values in the 3-D meshes for times T^k and T^l. For example, $G_{10,20}^{3,4}$ is the length of the ray path for the tenth measurement ($i = 10$) in the third data set ($k = 3$) attributed to node 20 ($j = 20$) in the fourth time-lapse 3-D mesh ($l = 4$). To construct the ray path matrix, we must first determine the influence of each nodal value on each predicted measurement. A ray path matrix element is calculated as the nodal weight (equation (5)) integrated numerically along the ray path R_i:

$$G_{ij}^{k,l}=\int_{R_i}w_j^l\left(\mathbf{r},t_i^k\right)d\mathbf{r}\approx\sum_{m=1}^{nsteps}w_j^l\left(\mathbf{x}_s+(m-1/2)\Delta\mathbf{x},t_i^k\right)\|\,\Delta\mathbf{x}\,\| \tag{7}$$

where $n$steps is the number of increments for numerical integration from the source location $\mathbf{x}_S$ to the receiver location $\mathbf{x}_R$, and $\Delta\mathbf{x}$ is the increment vector.

4.4. Tomographic Inverse Method

[31] We invert the time-lapse tomographic data using the procedure of *Day-Lewis et al.* [2002]. Details of the method are summarized here. The method sequentially estimates

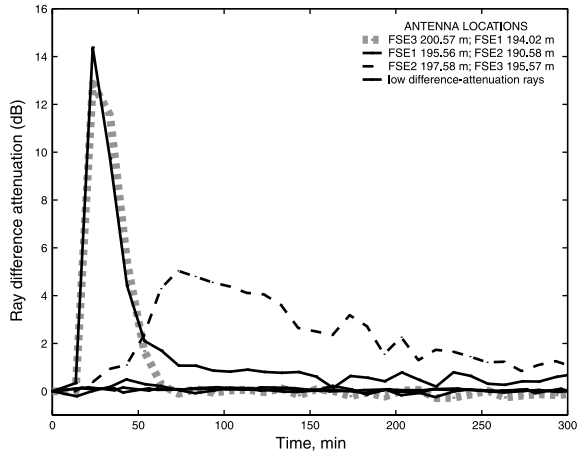

Figure 7. Difference attenuation for high- and low-attenuation rays in the three planes.

nodal parameters in each time mesh using data sets collected within a temporal window that contains the mesh. In this study, we use two time sets of data (i.e., $\mathbf{d}^{k-1}$ and $\mathbf{d}^{k}$) collected over a 20-min window to estimate the three time sets of parameters ($\Delta\boldsymbol{\alpha}^{k-1}$, $\Delta\boldsymbol{\alpha}^{k}$, and $\Delta\boldsymbol{\alpha}^{k+1}$) on which the data depend. The forward model is $\boldsymbol{\delta}^k = \boldsymbol{\Gamma}^k\mathbf{m}^k$:

$$\left[\frac{\mathbf{d}^{k-1}}{\mathbf{d}^{k}}\right] = \left[\frac{\mathbf{G}^{k-1,k-1}}{\mathbf{0}}\middle|\frac{\mathbf{G}^{k-1,k}}{\mathbf{G}^{k,k}}\middle|\frac{\mathbf{0}}{\mathbf{G}^{k,k+1}}\right]\left[\frac{\Delta\mathbf{a}^{k-1}}{\frac{\Delta\mathbf{a}^{k}}{\Delta\mathbf{a}^{k+1}}}\right] \tag{8}$$

[32] In each step of the tomographic inversion, we minimize the objective function Z, a combination of the sum of weighted squared data residuals and a measure of solution complexity based on an a priori covariance model:

$$Z = \left(\boldsymbol{\delta}^k - \boldsymbol{\Gamma}^k\ \hat{\mathbf{m}}^k\right)^T\mathbf{V}^{-1}\left(\boldsymbol{\delta}^k - \boldsymbol{\Gamma}^k\hat{\mathbf{m}}^k\right) + \left(\hat{\mathbf{m}}^k - \mathbf{X}\boldsymbol{\beta}\right)^T \cdot \mathbf{Q}^{-1}\left(\hat{\mathbf{m}}^k - \mathbf{X}\boldsymbol{\beta}\right), k = 1, n\text{steps} \tag{9}$$

where

- $\boldsymbol{\delta}^k$ data vector containing two time sets of data for step k of the inversion;
- $\boldsymbol{\Gamma}^k$ data kernel for step k of the inversion, corresponding to two time sets of data and three time meshes of nodes;
- $\hat{\mathbf{m}}^k$ vector of model parameter estimates for three time meshes of nodes in step k of the inversion;
- $\mathbf{V}$ diagonal matrix with elements equal to the error variances of $\boldsymbol{\delta}$;
- $\mathbf{Q}$ covariance matrix for model parameters $\hat{\mathbf{m}}^k$;
- $\mathbf{X}$ matrix defining the assumed, deterministic zonation and mathematical form of the mean (e.g., a constant or linear trend);
- $\boldsymbol{\beta}$ mean values determined by the inversion.

As the index k is incremented, the window in which parameters are estimated advances in time. Each time set of parameters is estimated in three steps, and the final estimate is taken as a weighted average of the three estimate vectors using a triangula hting scheme, i.e., weights of 1/4, 1/2, and 1/4. This averaging process amounts to applying a temporal smoother within the estimation process, thus reducing the effect of data errors present in single time steps, but also degrading the match to the data. This is similar to the application of spatial smoothers, such as the Hanning filter, to reduce inversion artifacts in tomograms [e.g., *Hyndman et al.*, 1994].

[33] We use a variable space-time mean, $\mathbf{X}\beta$, found by the inversion, to account for large differences in solute concentration in different planes. One mean value is used for the FSE1-FSE2 and FSE3-FSE1 planes, and another is used for the FSE2-FSE3 plane. Temporal changes in the means are partly accounted for by the sequential estimation, which allows the mean values to change from one step of the inversion to the next. Data errors are assumed uncorrelated and equal for all measurements collected in the same plane.

[34] The vector of parameter estimates, $\hat{\mathbf{m}}^k$, that minimize (9) is determined by solving the linear system

$$\left[\boldsymbol{\Gamma}^{k^T}\mathbf{V}^{-1}\boldsymbol{\Gamma}^k + \mathbf{M}\right]\hat{\mathbf{m}}^k = \boldsymbol{\Gamma}^{k^T}\mathbf{V}^{-1}\boldsymbol{\delta}^k \tag{10}$$

where

$$\mathbf{M} = \mathbf{Q}^{-1} - \mathbf{Q}^{-1}\mathbf{X}\left(\mathbf{X}^T\mathbf{Q}^{-1}\mathbf{X}\right)^{-1}\mathbf{X}^T\mathbf{Q}^{-1} \tag{11}$$

We solve the linear system (10) for $\hat{\mathbf{m}}^k$ using LU decomposition and then back solve for different right-hand sides in each step of the inversion. If the same transmitter-receiver geometry is used in every time step, a single LU decomposition is required.

[35] In under-determined problems, poor model resolution may result in streaking or blurring of geophysical anomalies, thus complicating interpretation of tomographic results. To reduce inversion artifacts, we utilize additional information in the form of ray-based constraints that restrict difference-attenuation anomalies to regions crossed by ray paths along which significant attenuation changes are observed. The criteria for applying zero-value constraints are established and applied separately for each plane. In a given plane, a ray path is designated as being affected by tracer if, in any time set of data, the ray path shows a positive difference attenuation greater than a cutoff, P_{high}. Similarly, unaffected ray paths are those that are always below a second cutoff, P_{low}. We use high and low cutoffs corresponding to the 97th percentile and the mean of the data in the time set exhibiting the greatest difference-attenuation for the given plane. Selection of appropriate cutoffs was guided by inspection of ray path plots, such as Figure 6; other values may be appropriate for different data sets.

[36] On the basis of the spatial configuration of high and low difference-attenuation ray paths, nodes are sorted into three categories: (1) nodes inside or adjacent to regions traversed by high difference-attenuation ray paths; (2) nodes within an additional two row or column spacings of the region affected by tracer migration; and (3) other nodes unaffected by tracer migration. Nodes in the third category are not included in the inversion, but are implicitly constrained to zero difference attenuation. Nodes in the second category are included as parameters in the inversion but constrained to zero difference attenuation using Lagrange

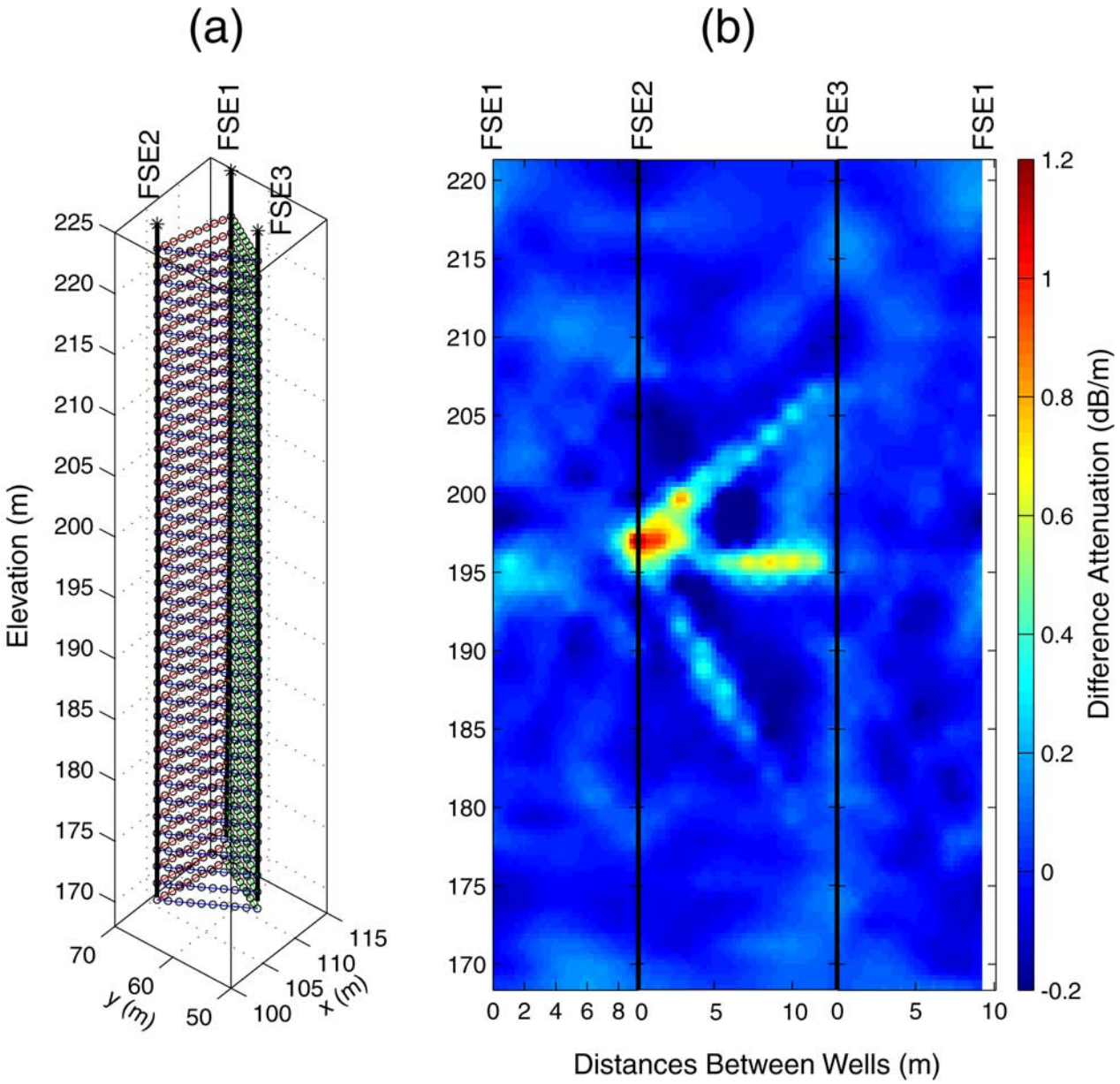

Figure 8. (a) The 3-D nodal mesh used for inversion, and (b) the 90-min difference-attenuation tomograms from unconstrained inversion. The planes of the three-well prism are unfolded in the display of tomograms.

multipliers to ensure smooth variation between the active and zero-value regions. Nodes in the first category are retained as active parameters for every step of the sequential inversion.

[37] The solution for the constrained problem, $\hat{\mathbf{m}}^{k'}$, is determined by solving the linear system

$$\begin{bmatrix} \boldsymbol{\Gamma}^{k^T}\mathbf{V}^{-1}\boldsymbol{\Gamma}^{k} + \mathbf{M} & \mathbf{F}^T \\ \mathbf{F} & \mathbf{0} \end{bmatrix} \begin{bmatrix} \hat{\mathbf{m}}^{k'} \\ \boldsymbol{\lambda} \end{bmatrix} = \begin{bmatrix} \boldsymbol{\Gamma}^{k^T}\mathbf{V}^{-1}\boldsymbol{\delta}^{k} \\ \mathbf{0} \end{bmatrix} \tag{12}$$

where $\boldsymbol{\lambda}$ is the vector of Lagrange multipliers and $\mathbf{F}\hat{\mathbf{m}}^{k'} = \mathbf{0}$ are the nodal constraints. The minimization of Z (equation (12)) is identical to the estimation step in the "geostatistical approach" used for hydrogeologic parameter estimation with a spatiall able mean [e.g., *Kitanidis and Vomvoris*, 1983; *Kitanidis*, 1995, 1996] with additional constraints. *Day-Lewis et al.* [2002] present formulae to compute the approximate inverses and resolution matrices for the unconstrained and constrained versions of this approach.

[38] The space-time covariance is modeled as the product of separable spatial and temporal spherical correlation functions [e.g., *Rouhani and Myers*, 1990]:

$$Q(h,\tau) = Q_o \rho_{xyz}(h)\rho_t(\tau) \tag{13}$$

where

$Q(h, \tau)$ space-time covariance;

$\rho_{xyz}(h)$ spatial correlation function, equal to $1 - [(3/2)\,(h/a_{xyz}) - (1/2)\,(h/a_{xyz})^3]$ if $h < a_{xyz}$, and 0 otherwise;

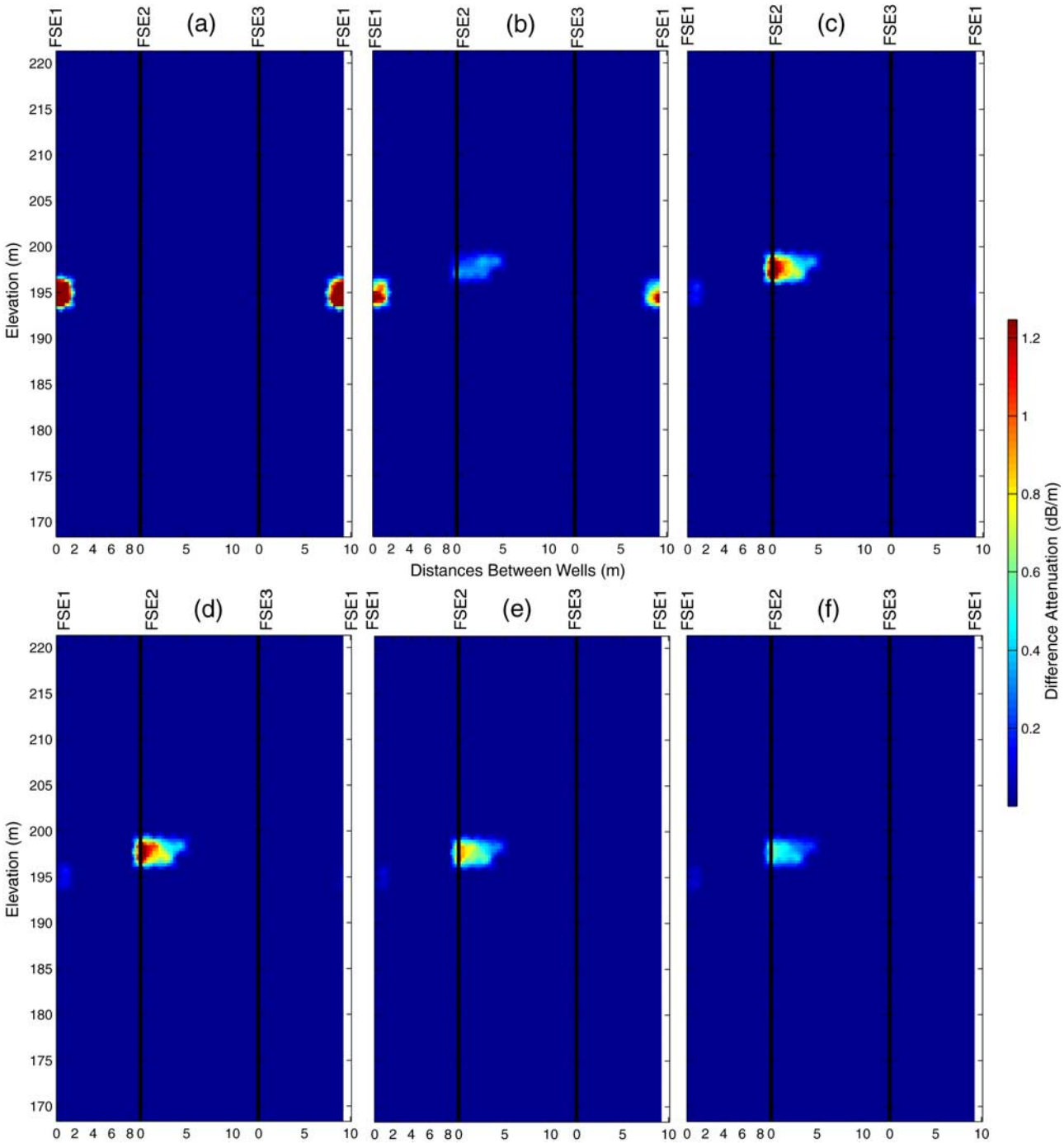

Figure 9. Shown are (a) 20-min, (b) 50-min, (c) 90-min, (d) 120-min, (e) 150-min, and (f) 200-min difference-attenuation tomograms from constrained inversion.

$\rho_t(\tau)$ temporal correlation function, equal to $1 - [(3/2)(\tau/a_t) - (1/2)(\tau/a_t)^3]$ if $\tau < a_t$, and 0 otherwise;
a_{xyz}, a_t spatial and temporal correlation ranges, respectively;
Q_o variance;
h spatial separation distance;
τ temporal separation.

We selected values for the variance (Q_0) as well as the ranges (a_{xyz} and a_t) of the covariance model that resulted in good data reproduction and smooth tomograms. Selection was made by trial-and-e ith qualitative analysis of the

Table 1. Inversion Parameters for Tomograms Shown in Figure 7 and Figure 8

Parameter	Value
a_{xyz}	15 m
a_t	150 min
Variance of $\Delta\alpha$	0.01 dB^2/m^2
Standard error:	
Plane 1	0.25 dB
Plane 2	0.13 dB
Plane 3	0.25 dB

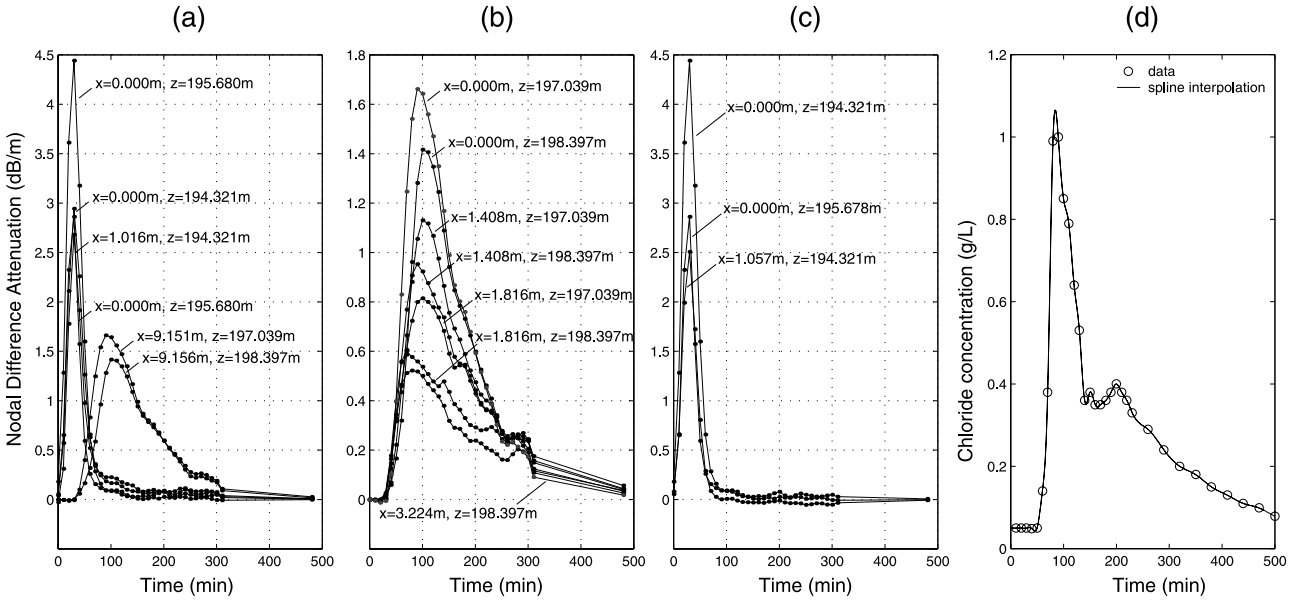

Figure 10. Nodal difference-attenuation histories in the (a) FSE1-FSE2, (b) FSE2-FSE3, and (c) FSE3-FSE1 image planes. Node locations are indicated as distance between wells (m) and elevation (m), for comparison with Figures 8 and 9. (d) Discharge concentration at FSE4.

resulting tomograms and fit to data. Selection of model parameters by the maximum likelihood method [*Kitanidis and Lane*, 1986] is an avenue of future research. It may be possible to identify covariance parameters for stochastic estimation or simulation of lithologic or hydraulic properties based on tomographic data.

5. Results and Discussion

[39] Our results include (1) difference-tomogram time series for unconstrained and constrained inversion, and (2) nodal difference attenuation histories indicating the timing of tracer breakthrough.

5.1. Difference Tomograms

[40] Tomographic inversion of the radar data yields a time series of 31 tomograms for the FSE1-FSE2, FSE2-FSE3, and FSE3-FSE1 planes. Results for unconstrained time-lapse inversion (10) include streak artifacts due to poor model resolution (Figure 8), but unambiguously indicate the presence of high difference-attenuation anomalies in all three planes: near the injection interval in the FSE1-FSE2 and FSE3-FSE1 planes, and near FSE2 in the FSE2-FSE3 plane. In constrained inversion (12), the application of ray-based constraints enhances image resolution and increases the magnitude of the anomalies (Figure 9). Inversion parameters for these solutions are given in Table 1. For each plane, the assumed standard data error was based on the standard deviation of measurements during several time-steps when no anomaly was present (late-time for FSE1-FSE2 and FSE3-FSE1, and early time for FSE2-FSE3).

[41] From the tomographic results, we make three inferences regarding the spatial distribution of tracer transport. First, the anomaly in the FSE1-FSE2 and FSE3-FSE1 planes remains close to the injection interval, indicating the tracer plume travels only a sho tance before leaving these planes. Second, transport is channelized along a preferential pathway that intersects the FSE2-FSE3 plane in the vicinity of FSE2. Third, it is probable that much of the tracer is leaving the three-well prism; thus we cannot assume that all the tracer mass crosses the FSE2-FSE3 plane, and accurate moment or mass balance calculations are not possible. These results are consistent with preliminary insights based on exploratory data analysis (section 4.1).

5.2. Nodal Difference-Attenuation Histories

[42] Estimation of solute breakthrough curves from time-lapse tomograms [e.g., *Binley et al.*, 1996; *Slater et al.*, 2000] can provide valuable information for calibration of ground-water flow and transport models. Difference-attenuation histories corresponding to the constrained inversion are plotted in Figure 10 for nodes in the FSE1-FSE2, FSE2-FSE3, and FSE3-FSE1 planes. The tracer concentration in the FSE4 discharge is plotted in Figure 10d for comparison. The tracer is undetected in the FSE1-FSE2 and FSE3-FSE1 planes about 90 min after injection (Figures 10a and 10c, respectively). Although the first detection in the FSE2-FSE3 plane (~30 min) is reasonable compared to the first detection at the outlet (~50 min), the timing of the peak difference attenuation is harder to explain. Nodal difference-attenuation histories in the FSE2-FSE3 plane (Figure 10b) indicate that the timing of the tracer peak is between 80 and 100 min after injection, yet the tracer concentration at the outlet peaks earlier, at about 77 min. Furthermore, we would expect the breakthrough curve at the outlet to be broader than the breakthrough curve at points in the FSE2-FSE3 plane where the effect of dispersion should be less, yet we observe the opposite.

[43] We suggest several hypotheses to explain the apparent inconsistency between difference-attenuation tomograms and measured tracer concentration. First, it is possible that much of the tracer leaves the three-well prism, and that

the anomaly in the FSE2-FSE3 plane represents a slower pathway. This would explain both the peak timing discrepancy and the broadness of the difference-attenuation curves. A second factor is scale. Because of local averaging and finite-measurement support, tomographic estimates may be affected by transport along multiple paths, some fast and some slow. Thus the difference-attenuation history of a node would approximate a composite history for multiple paths, peaking later than the fastest path and earlier than the slowest. A third issue is rate-limited mass transfer (RLMT). In the presence of RLMT, solute is present in both mobile and immobile porosity [e.g., *Harvey and Gorelick*, 2000]. Whereas discharge measurements of concentration sample preferentially from mobile porosity, the radar would be sensitive to salt in both mobile and immobile domains. Again, this could affect both the peak timing and shape of the difference-attenuation breakthrough. These possibilities are explored by F. D. Day-Lewis et al. (Combined interpretation of radar, hydraulic and tracer data from a fractured-rock aquifer, submitted to *Hydrogeology Journal*, 2003; hereinafter referred to as submitted manuscript, 2003), where a suite of flow and transport models are calibrated to hydraulic and tracer data. The conceptual models explored included combinations of RLMT and different patterns of zonal heterogeneity based on the geophysical results presented here. The experimental data are shown to be consistent with simple zonal heterogeneity that diverts tracer to the edge of and outside of the three-well prism.

6. Conclusions

[44] We demonstrated sequential inversion of cross-well radar data from a field experiment at the U.S. Geological Survey Fractured-Rock Hydrology Research Site in Grafton County, New Hampshire. Time-lapse difference-attenuation data were collected in three planes that form a triangular prism between three boreholes. Whereas preliminary analyses of the field data [*Lane et al.*, 1998; *Lane et al.*, 2000] yielded tomograms containing artifacts that complicated hydrologic interpretation, we show that sequential time-lapse inversion provides unambiguous, high-resolution images of tracer transport between wells. This is achieved by (1) capitalizing on temporal correlation to regularize the inversion, (2) accounting for the timing of measurements, and (3) applying ray-based constraints to restrict the location and extent of the target anomaly. This effort represents the first application of the sequential inversion approach of *Day-Lewis et al.* [2002] to field data. The experimental results provide basic and site-specific insights into groundwater flow and solute transport in fractured rock. From the tomograms, we identified a preferential flow path inside a previously identified fracture zone and estimated the timing of peak tracer occurrence in the image planes. On the basis of hydraulic data alone, the fracture zone might appear internally homogeneous; however, the time-lapse difference-attenuation tomograms indicate significant spatial variability within the fracture zone. On the basis of the geophysical results, the tracer migrates along a preferential pathway at the edge of the three-well prism. The geophysical results provide valuable new information to construct and calibrate high-resolution numerical models of groundwater flow and solute tr t. The apparent inconsistency between the timing of peak difference attenuation and outlet concentration is a topic of an ongoing modeling study (F. D. Day-Lewis et al., submitted manuscript, 2003). Plausible explanations include (1) diversion of tracer outside the three-well prism, (2) the measurement support volume and effect of local averaging in the inversion, and (3) rate-limited mass transfer.

[45] **Acknowledgments.** This material is based upon work supported by the National Science Foundation under Grant Nos. EAR-0124262 and EAR-9705812. Any opinions, findings, and conclusions or recommendations expressed in this material are those of the author(s) and do not necessarily reflect the views of the National Science Foundation. Additional support was provided by the U.S. Geological Survey's Toxic Substances Hydrology Program and the U.S. Environmental Protection Agency through EPA STAR Fellowship U-915155-01-0. We are grateful for technical reviews by Kamini Singha, Karl Ellefsen, two anonymous reviewers, and the anonymous associate editor.

References

Archie, G. E., The electrical resistivity log as an aid in determining some reservoir characteristics, *Trans. Am. Inst. Min. Metall. Pet. Eng.*, *146*, 54–62, 1942.

Bachrach, R., and A. Nur, High-resolution shallow seismic experiments in sand, part 1, Water table, fluid flow, and saturation, *Geophysics*, *63*(4), 1225–1233, 1998.

Becker, M. W., and A. M. Shapiro, Tracer transport in fractured crystalline rock: Evidence of nondiffusive breakthrough tailing, *Water Resour. Res.*, *36*(7), 1677–1686, 2000.

Becker, W. M., and A. M. Shapiro, Interpreting tracer breakthrough tailing from different forced-gradient tracer experiment configurations in fractured bedrock, *Water Resour. Res.*, *39*(1), 1024, doi:10.1029/2001WR001190, 2003.

Binley, A., S. Henry-Poulter, and B. Shaw, Examination of solute transport in an undisturbed soil column using electrical resistance tomography, *Water Resour. Res.*, *32*(4), 763–769, 1996.

Binley, A., W. Daily, and A. Ramirez, Detecting leaks from environmental barriers using electrical current imaging, *J. Environ. Eng. Geophys.*, *2*(1), 11–19, 1997.

Binley, A., P. Winship, R. Middleton, M. Pokar, and J. West, High-resolution characterization of vadose zone dynamics using cross-borehole radar, *Water Resour. Res.*, *37*(11), 2639–2652, 2001.

Bregman, N. D., R. C. Bailey, and C. H. Chapman, Crosshole seismic tomography, *Geophysics*, *54*(2), 200–215, 1989a.

Bregman, N. D., R. C. Bailey, and C. H. Chapman, Ghosts in tomography: The effects of poor angular coverage in 2-D seismic travel time inversion, *Can. J. Explor. Geophys.*, *25*(1), 7–27, 1989b.

Brewster, M. L., and A. P. Annan, Ground-penetrating radar monitoring of a controlled DNAPL release: 200 MHz radar, *Geophysics*, *59*(8), 1211–1221, 1994.

Brewster, M. L., A. P. Annan, J. P. Greenhouse, B. H. Kueper, G. R. Olhoeft, J. D. Redman, and K. A. Sander, Observed migration of a controlled DNAPL release by geophysical methods, *Ground Water*, *33*(6), 977–987, 1995.

Burkhart, T., A. R. Hoover, and P. B. Flemings, Time-lapse (4-D) seismic monitoring of primary production of turbidite reservoirs at South Timbalier Block 295, offshore Louisiana, Gulf of Mexico, *Geophysics*, *65*(2), 351–367, 2000.

Censor, Y., Finite series-expansion reconstruction methods, *Proc. IEEE*, *71*(3), 409–419, 1983.

Daily, W., Underground oil-shale retort monitoring using geotomography, *Geophysics*, *49*, 1701–1707, 1984.

Daily, W., and A. Ramirez, Evaluation of electromagnetic tomography to map in situ water in heated welded tuff, *Water Resour. Res.*, *25*(6), 1083–1096, 1989.

Dakhnov, V. N., Geophysical well logging, *Q. Colo. Sch. Mines*, *57*(2), 109, 1962.

Davis, J. L., and A. P. Annan, Ground-penetrating radar for high-resolution mapping of soil and rock stratigraphy, *Geophys. Prospect.*, *37*, 531–551, 1989.

Day-Lewis, F. D., P. A. Hsieh, and S. M. Gorelick, Identifying fracture-zone geometry using simulated annealing and hydraulic-connection data, *Water Resour. Res.*, *36*(7), 1701–1721, 2000.

Day-Lewis, F. D., J. M. Harris, and S. M. Gorelick, Time-lapse inversion of cross-well radar data, *Geophysics*, *67*(6), 1740–1752, 2002.

Dines, K. A., and R. J. Lytle, Computerized geophysical tomography, *Proc. IEEE*, *67*, 1065–1073, 1979.

Eppstein, M. J., and D. E. Dougherty, Efficient three-dimensional data inversion: Soil characterization and moisture monitoring from cross-well ground-penetrating radar at a Vermont test site, *Water Resour. Res.*, *34*(8), 1889–1900, 1998a.

Eppstein, M. J., and D. E. Dougherty, Optimal 3-D travel time tomography, *Geophysics*, *63*(3), 1053–1061, 1998b.

Harris, J. M., Y. Feng, and Y. Quan, Enhanced oil recovery monitoring using *P*-wave attenuation, in *SEG Annual Meeting Expanded Technical Program Abstracts With Biographies*, vol. 66, pp. 1882–1885, Soc. of Explor. Geophys., Tulsa, Okla., 1996a.

Harris, J. M., R. T. Langan, T. G. Fasnacht, D. Melton, B. Smith, J. Sinton, and H. Tan, Experimental verification of seismic monitoring of CO_2 injection in carbonate reservoirs, in *SEG Annual Meeting Expanded Technical Program Abstracts With Biographies*, vol. 66, pp. 1870–1872, Soc. of Explor. Geophys., Tulsa, Okla., 1996b.

Harvey, C. F., and S. M. Gorelick, Rate-limited mass transfer or macrodispersion: Which dominates plume evolution at the macrodispersion experiment (MADE) site?, *Water Resour. Res.*, *36*(3), 637–650, 2000.

Hsieh, P. A., and A. M. Shapiro, Hydraulic characteristics of fractured bedrock underlying the FSE well field at the Mirror Lake Site, Grafton County, New Hampshire, in *U.S. Geological Survey Toxic Substances Hydrology Program: Proceedings of the Technical Meeting, Colorado Springs, Colorado, September 20–24, 1993*, edited by D. W. Morganwalp and D. A. Aronson, *U.S. Geol. Surv. Water Resour. Invest. Rep., 94-4015*, *1*, 127–130, 1996.

Hsieh, P. A., A. M. Shapiro, and C. R. Tiedeman, Computer simulation of fluid flow in fractured rocks at the Mirror Lake FSE well field, in *U.S. Geological Survey Toxic Substances Hydrology Program: Proceedings of the Technical Meeting, Charleston, South Carolina, March 8–12, 1999: Subsurface Contamination from Point Sources*, edited by D. W. Morganwalp and H. T. Buxton, *U.S. Geological Surv. Water Resour. Invest. Rep., 99-4018C*, 777–781, 1999.

Hubbard, S., J. Chen, J. Peterson, E. Majer, K. Williams, D. Swift, B. Mailliox, and Y. Rubin, Hydrogeological characterization of the D.O.E., bacterial transport site in Oyster Virginia using geophysical data, *Water Resour. Res.*, *37*(10), 2431–2456, 2001.

Hyndman, D. W., and J. M. Harris, Travel time inversion for the geometry of aquifer lithologies, *Geophysics*, *61*(6), 1728–1737, 1996.

Hyndman, D. W., J. M. Harris, and S. M. Gorelick, Coupled seismic and tracer test inversion for aquifer property characterization, *Water Resour. Res.*, *30*(7), 1965–1977, 1994.

Isaaks, E. H., and R. M. Srivastava, *Applied Geostatistics*, Oxford Univ. Press, New York, 1989.

Kitanidis, P. K., Quasi-linear geostatistical theory for inversing, *Water Resour. Res.*, *31*(10), 2411–2419, 1995.

Kitanidis, P. K., On the geostatistical approach to the inverse problem, *Adv. Water Resour.*, *19*(6), 333–342, 1996.

Kitanidis, P. K., and R. W. Lane, Uncertainty in estimation of spatial functions: Bayesian analysis, *Water Resour. Res.*, *22*(6), 984–986, 1986.

Kitanidis, P. K., and E. G. Vomvoris, A geostatistical approach to the inverse problem in groundwater modeling (steady state) and one-dimensional simulations, *Water Resour. Res.*, *19*(3), 677–690, 1983.

Lane, J. W. Jr., F. P. Haeni, and F. D. Day-Lewis, Use of time-lapse attenuation-difference radar tomography methods to monitor saline tracer transport in fractured crystalline bedrock, in *Proceedings of the Seventh International Conference on Ground Penetrating Radar*, vol. 2, pp. 533–538, Radar Syst. and Remote Sens. Lab., Univ. of Kans., Lawrence, 1998.

Lane, J. W. Jr., F. D. Day-Lewis, J. M. Harris, F. P. Haeni, and S. M. Gorelick, Attenuation-difference radar tomography: Results of a multiple-plane experiment at the Geological Survey Fractured Rock Research Site, U.S., Mirror Lake, New Hampshire, in *Proceedings of the Eighth International Conference on Ground Penetrating Radar*, edited by D. A. Noon, G. F. Stickely, and D. Longstaff, *Proc. SPIE Int. Soc. Opt. Eng., 4084,* 666–675, 2000.

Lane, J. W. Jr., F. D. Day-Lewis, R. J. Versteeg, and C. C. Casey, Object based inversion of cross-well radar tomography data to monitor vegetable oil injection experiments, in *Symposium on the Application of Geophysics to Engineering and Environmental Problems* (*SAGEEP*) [CD-ROM], pp. 1134–1160, Environ. and Eng. Geophys. Soc., Denver, Colo., 2003.

Maurer, H., and K. Holliger, Stochastic regularization: Smoothness or similarity?, *Geophys. Res. Lett.*, *25*(15), 2889–2892, 1998.

Menke, W., *Geophysical Data Analysis: Discrete Inverse Theory*, rev. ed., Academic, San Diego, Calif., 1989.

Michelena, R., and J. M. Harris, Tomographic travel time inversion using natural pixels, *Geophysics*, *56*(5), 635–644, 1991.

National Research Council, *Rock Fractures and Fluid Flow*, Natl. Acad. Press, Washington, D.C., 1996.

Niva, B., O. Olsson, and P. Blumping, Radar cross-hole tomography at the Grimsel Rock Laboratory with application to migration of saline tracer through fracture zones, *Tech. Rep. 88-311*, Natl. Coop. for the Storage of Radioactiv. Waste, Baden, Switzerland, 1988.

Nolet, G., *Seismic Tomography*, D. Riedel, Norwell, Mass., 1987.

Olsson, O., P. Anderson, and E. Gustafsson, Site characterization and validation-Monitoring of saline tracer transport by borehole radar measurements, final report, *Stripa Proj. TR91-18*, Swed. Nucl. Fuel and Waste Manage. Co., Stockholm, 1991.

Olsson, O., L. Falk, O. Forslund, L. Lundmark, and E. Sandberg, Borehole radar applied to the characterization of hydraulically conductive fracture zones in crystalline rock, *Geophys. Prospect.*, *40*(2), 109–142, 1992.

Osiensky, J. L., and P. R. Donaldson, Electrical flow through an aquifer for contaminant source leak detection and delineation of plume evolution, *J. Hydrol.*, *169*(1–4), 243–263, 1995.

Ramirez, A. L., and R. J. Lytle, Investigation of fracture flow paths using alterant geophysical tomography, *Int. J. Rock. Mech. Min. Sci. Geomech. Abstr.*, *23*, 165–169, 1986.

Ramirez, A., W. Daily, D. LaBrecque, E. Owen, and D. Chestnut, Monitoring an underground steam injection process using electrical resistance tomography, *Water Resour. Res.*, *29*(1), 73–87, 1993.

Ramirez, A., W. Daily, A. M. Binley, A. LaBrecque, and D. Roelant, Detection of leaks in underground storage tanks using electrical resistance methods, *J. Environ. Eng. Geophys.*, *1*(3), 189–203, 1996.

Rector, J. W., and J. K. Washbourne, Characterization of resolution and uniqueness in cross-well direct-arrival travel time tomography using the Fourier projection slice theorem, *Geophysics*, *59*(11), 1642–1649, 1994.

Rouhani, S., and D. E. Myers, Problems in spatiotemporal kriging of geohydrological data, *Math. Geol.*, *22*(5), 611–623, 1990.

Schuster, G. T., Resolution limits for cross-well migration and travel time tomography, *Geophys. J. Int.*, *127*, 427–440, 1996.

Singh, R. P., and Y. P. Singh, RAYPT: A new inversion technique for geotomographic data, *Geophysics*, *56*(8), 1215–1227, 1991.

Singha, K., A. M. Binley, J. W. Lane, Jr., and S. M. Gorelick, Electrical imaging of tracer migration at the Massachusetts Military Reservation, Cape Cod, in *Symposium on the Application of Geophysics to Engineering and Environmental Problems* (*SAGEEP*) [CD-ROM], pp. 464–474, Environ. and Eng. Geophys. Soc., Denver, Colo., 2003.

Slater, L. D., and S. K. Sandberg, Resistivity and induced polarization monitoring of salt transport under natural hydraulic gradients, *Geophysics*, *65*(2), 408–420, 2000.

Slater, L., A. Binley, and D. Brown, Electrical imaging of the response of fractures to ground water salinity change, *Ground Water*, *35*(3), 436–442, 1997.

Slater, L., A. M. Binley, W. Daily, and R. Johnson, Cross-hole electrical imaging of a controlled saline tracer injection, *J. Appl. Geophys.*, *44* (2–3), 85–102, 2000.

Stratton, J. A., *Electromagnetic Theory*, McGraw-Hill, New York, 1941.

Tsang, Y. W., and C. F. Tsang, Flow channeling in a single fracture as a two-dimensional strongly heterogeneous permeable medium, *Water Resour. Res.*, *25*(9), 2076–2080, 1989.

Vesnaver, A., and G. Böhm, In quest of the grid, *Geophysics*, *64*(4), 1116–1125, 1999.

Vesnaver, A., and G. Böhm, Staggered or adapted grids for seismic tomography, *Leading Edge*, *19*, 944–950, 2000.

White, P. A., Measurement of ground-water parameters using salt-water injection and surface resistivity, *Groundwater*, *26*(2), 179–186, 1988.

Williamson, P. R., and M. H. Worthington, Resolution limits in ray tomography due to wave behavior: Numerical experiments, *Geophysics*, *58*(5), 727–735, 1993.

F. D. Day-Lewis and J. W. Lane, Jr., Office of Groundwater, Branch of Geophysics, U.S. Geological Survey, 11 Sherman Place, U-5015, Storrs, CT 06269, USA. (fdaylewi@bucknell.edu)

S. M. Gorelick, Department of Geological and Environmental Sciences, Building 320, Braun Geology Corner, Stanford University, Stanford, CA 94305, USA.

J. M. Harris, Department of Geophysics, Mitchell Building, Stanford University, Stanford CA 94305, USA.